We are IntechOpen,
the world's leading publisher of Open Access books
Built by scientists, for scientists

4,800
Open access books available

122,000
International authors and editors

135M
Downloads

154
Countries delivered to

Our authors are among the

TOP 1%
most cited scientists

12.2%
Contributors from top 500 universities

BOOK CITATION INDEX
CLARIVATE ANALYTICS
INDEXED

WEB OF SCIENCE™

Selection of our books indexed in the Book Citation Index
in Web of Science™ Core Collection (BKCI)

Interested in publishing with us?
Contact book.department@intechopen.com

Electrodeposition of Ferromagnetic Nanostructures

Monika Sharma and Bijoy K. Kuanr

Additional information is available at the end of the chapter

Abstract

The fabrication of one-dimensional ferromagnetic nanostructured materials such as nanowires and nanotubes by the electrodeposition technique is discussed. The size, shape and structural properties of nanostructures are analysed by controlling the deposition parameters such as precursors used, deposition potential, pH, etc. The growth of nanostructures and various characterization techniques are studied to support their one-dimensionality. A comparative study of ferromagnetic nanowires and nanotubes is made using angular-dependent ferromagnetic resonance technique.

Keywords: Electrodeposition, nanowires, nanotubes, ferromagnetic resonance, anodic aluminium oxide

1. Introduction

Recently, one-dimensional ferromagnetic nanostructured materials such as nanodots, anti-dots, nanowires and nanotubes have attracted intense research interest. These nanostructures have potential applications in fields as diverse as data storage, magnetics, electronics, optical and microwave devices and nanomedicine [1-6]. They often exhibit new and enhanced properties, due to their low-dimensionality and inter-wire interaction as compared to bulk materials. Several methods have been developed for the synthesis of one-dimensional (1D) nanostructures which lead to well-defined dimensions, morphology, crystal structure, and composition. Various methods such as electrochemistry, chemical reduction, vapour-liquid-solid growth, etc., have been used for preparation of magnetic nanostructures [7-9], although template electrodeposition constitutes one of the most general methods to achieve 1D growth [10-11]. Template-based approach allows to systematically vary the size, shape and structural properties of nanostructures through the modification of template and electrodeposition conditions [12]. The template-based growth often allows the growth of polycrystalline nature of nanowires and nanotubes; however, by controlling the various deposition parameters one

can easily overcome such issues and thus *single crystal nanostructures can be achieved*. Electrodeposition technique is also an inexpensive technique which allows the formation of periodically ordered nanostructures in periodic substrates, which enhances their use in potential device applications. The understanding of the growth mechanism would benefit the controlled fabrication of desired metal nanostructures for specific applications. In particular, nanostructures have been prepared in nanoporous membranes by triblock copolymer-assisted hard-template method [13], electroplating [14], a sequential electrochemical synthetic method [15] and nanoporous templates [16]. Fundamentally, nanowire growth depends upon electrodeposition parameters and nanotube formation is dependent on the different growth rates of the metal along the wall surface and from the central bottom of the nanochannels. However, systematic studies are still needed to understand the growth mechanism of nanowires and nanotubes.

Ferromagnetic nanowires and nanotubes exhibit unique and tunable magnetic properties due to their inherent shape anisotropy. Current interest in research on ferromagnetic nanowires and nanotubes is stimulated by their potential applications in different fields such as spintronics, biotechnology, future ultra-high-density magnetic recording media and high-frequency devices [17-21]. For applications such as magnetic recording media, the nanowire's diameter and the inter-wire distance should be as small as possible to increase the areal recording density. Thus, for storage devices magnetic studies concentrate on sub-100 nm nanostructures. The high aspect ratio of the nanowires (Length/Diameter) causes high coercivity, which is helpful in suppressing the onset of the 'superparamagnetic limit', which is considered to be very important for preventing the loss of magnetically recorded information among the nanowires. The inter-wire interaction and magnetic dipole coupling can be controlled by suitable separation among the nanowires.

Several groups have investigated elemental ferromagnetic nanowires such as Fe, Co and Ni with different pore diameters in alumina templates [12-21]. Huang et al. reported single crystal Co nanowires with different diameters and observed that the coercivity and squareness decreases with increase of pore diameter [22]. The size of the crystallites within the Fe, Co and Ni nanowires, as well as the crystalline structure of the nanowires, depends upon the deposition conditions such as the pH of the solutions and the deposition parameters. Giant-magneto-resistance (GMR) properties were found in Co/Cu multi-layered nanowires electrodeposited in nanoporous polymer template [23]. Recently, these ferromagnetic nanowire embedded templates were used as a substrate for making high-frequency devices [24-26].

In this chapter, we shall describe three different aspects of this topic:

1. We first discuss in brief about the template approach for fabricating one-dimensional nanostructures. The most commonly used templates, i.e. anodic alumina membrane (AAM) and polycarbonate (PC) membranes, will be discussed in detail.

2. We will then describe the electrochemical deposition technique used to synthesize ferromagnetic nanowire and nanotube arrays. The size, shape and structural properties of nanostructures are controlled by the type of template used and a number of growth parameters such as precursors used, deposition potential, pH, etc.

3. We will then continue discussing the various characterization techniques and physical properties of these nanostructures. A comparative study of ferromagnetic nanowires and nanotubes has been made using static and dynamic magnetization techniques.

2. Template-based approach

Template electrodeposition is one of the most general techniques to realize one-dimensional growth. In this straightforward approach, the nanostructures are grown electrochemically inside a hard-template material (mould) adopting its shape [27, 28]. Usually, a template (membrane) is a material that has pores of radii varying from a few μm to tens of nm. These porous membranes are generally used in filtration technologies for the separation of different species such as polymers, colloids, molecules, salts, etc. Anodic aluminium oxide (AAO) membrane and polycarbonate (PC) membranes are commonly used membranes for the synthesis of one-dimensional nanostructures [29, 30]. However, PC membranes are disadvantageous as they have random pores and are very flexible. During the heating process, these membranes can lead to distortion, which is one of the major drawbacks for device applications. Also, removal of the template occurs before complete densification of the nanostructures. These factors result in broken and deformed nanostructures. Anodic aluminium oxide (AAO) template overcomes these difficulties as these membranes have uniform and parallel pores and are therefore commonly used for synthesis of 1D nanostructures. Two-step anodization of aluminium sheet in acidic medium solutions of sulphuric, oxalic, or phosphoric acids is used to synthesize AAO templates [29, 31]. Depending upon the anodization conditions, pore densities as high as 10^{11} pores/cm^2 can be obtained and due to mechanical stress at the aluminium-alumina interface, these pores are arranged in a regular hexagonal array as shown in Fig. 1 [32]. A large array of orderly arranged pores with high aspect ratio makes AAO templates ideal for growing nanostructures. The thickness of the template, which determines the length of nanowires, only depends upon the oxidation time and can lead to formation of 1-60 μm thick oxide layers. AAO templates are chemically and thermally inert, causing pure synthesis of ferromagnetic materials. Also, the solution being deposited must wet the internal pore walls and for growth of nanotubules, deposition should start from the pore wall and should proceed inward.

In the anodization process, an electrical circuit is established between a cathode and a film of aluminium which serves as the anode. Then, anodic oxidation or anodization of the film occurs in accordance to the following reaction [33]:

$$2Al + 3H_2O = Al_2O_3 + 3H_2, \ \Delta G° = -864.6 \text{ kJ} \tag{1}$$
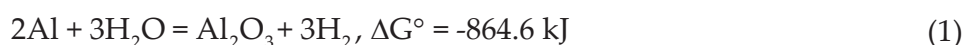
where $\Delta G°$ is the standard Gibbs free energy change. During the anodization, initially a planar barrier film forms followed by pore development leading to the formation of the relatively regular porous anodic film, which thickens in time.
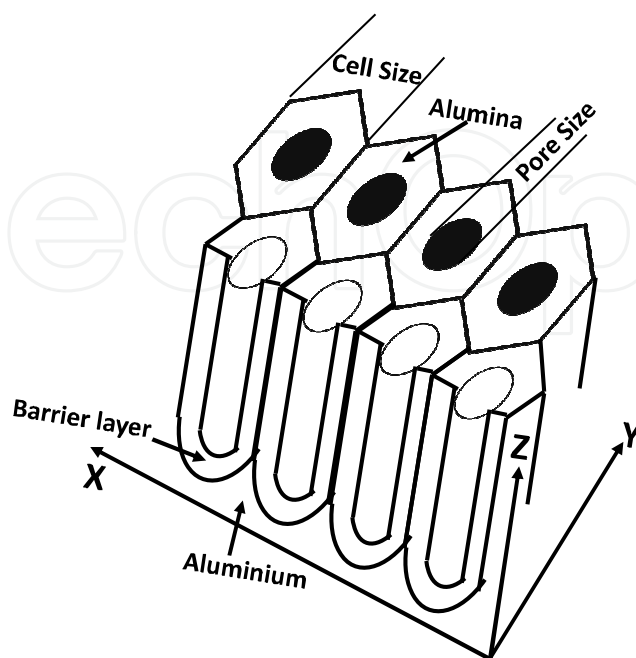
Figure 1. Schematic diagram of the cross section of the porous anodic aluminium oxide showing the nanopores arranged in hexagonal cells.

In two-step anodization, usually the first and second anodization steps could be conducted in the same conditions. The oxide layer formed in the first step is removed by wet chemical dissolution in a mixture of suitable chemicals for an appropriate time, depending on the anodizing time. Based on the applied anodizing voltage and also the type of electrolyte, pores with diameters ranging from few nm to 200 nm can be produced. Li et al. demonstrated a formula between inter-pore distance (D_{nm}) and anodizing voltage (V) [34]:

$$D_{nm} = -1.7 + 2.81 \, V \, (\text{volts}) \qquad (2)$$

High-purity (99.99%) aluminium (Al) foil was used for anodization. It was ultrasonically degreased at room temperature in trichloroethylene for 5 min, and then etched in 1.0 M NaOH for 3 min. Before anodization, Al foil was electrochemically polished in a mixed solution of $HClO_4$ and ethanol. A two-step anodization was used to obtain highly ordered pores. Al foil was anodized at 40 V in a 0.3 M oxalic acid at 0 °C for about 12 h in the first anodization step. The oxide layer formed in first anodization was chemically removed in a mixture of phosphoric acid and chromic acid which creates a footprint of nanopores on the Al surface. A second anodization was carried out with the same solutions and steps used in first anodization, resulting in the formation of highly ordered pores [29, 31].

In this chapter, we show results using the commercially purchased AAO templates from Whatman Ltd. and observe that these AAO templates were branched from one side (O-ring support side) as shown in Fig. 2.
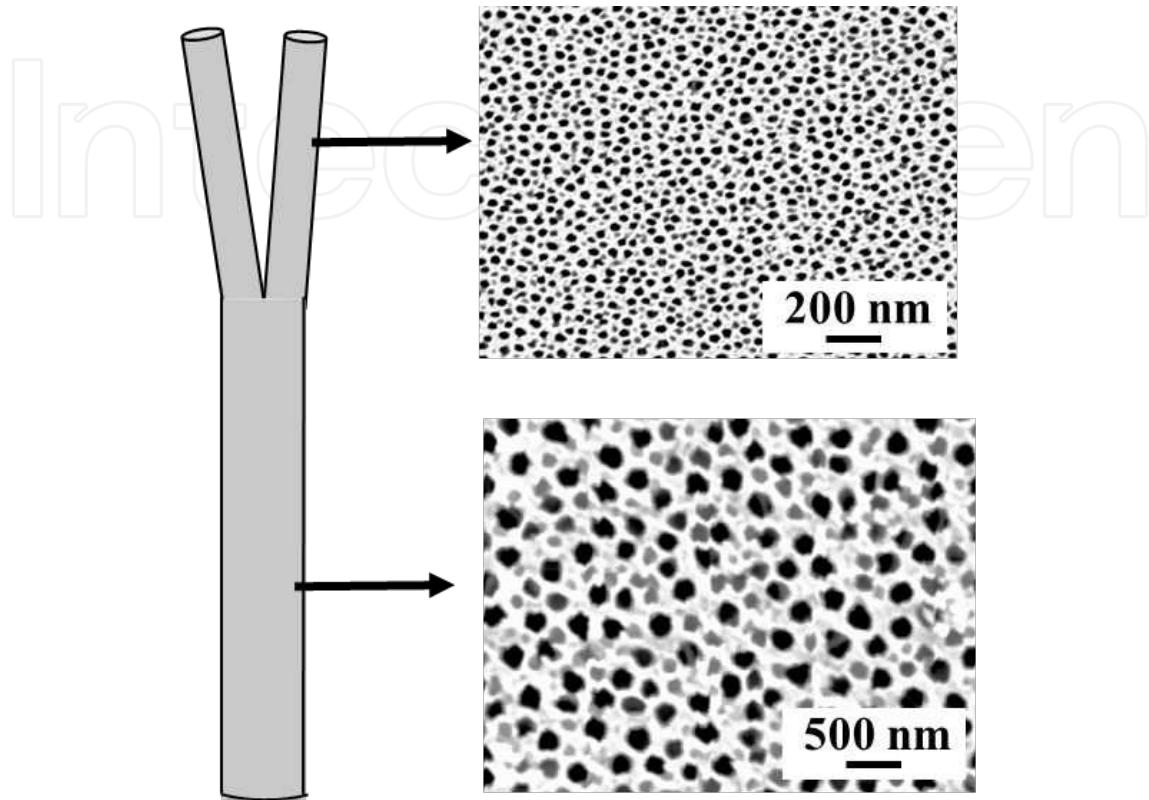

Figure 2. Branching observed in anodic alumina templates commercially available from Whatman.

3. Electrodeposition

Electrodeposition, also known as electrochemical deposition, is a process which involves the oriented diffusion of charged reactive species through a solution when an external electric field is applied, and the reduction of the charged growth species at the deposition surface. Surface charge will develop when a solid is immersed in a polar solvent or an electrolyte solution. The Nernst equation which described the electrode potential is given by

$$V = V_0 + \frac{RT}{n_i F} \ln(a_i) \tag{3}$$

where V_0 is the potential difference between the electrode and the solution for unity activity a_i of the ions, F is the Faraday's constant, R is the gas constant and T is the temperature.

Electrons will transfer from the electrode to the solution and the electrolyte will be reduced when the electrode potential is higher than the energy level of a vacant molecular orbital in the electrolyte, as shown in Fig. 3. On the other hand, electrolyte oxidation will occur, i.e. the electrons will transfer from the electrolyte to the electrode, if the electrode potential is lower than the energy level of an occupied molecular orbital in the electrolyte, as shown in Fig. 3. When equilibrium is achieved, these reactions will stop. Electrolysis is a process that converts electrical energy to chemical potential in an electrolytic cell where charged species flow from cathode to anode [35].
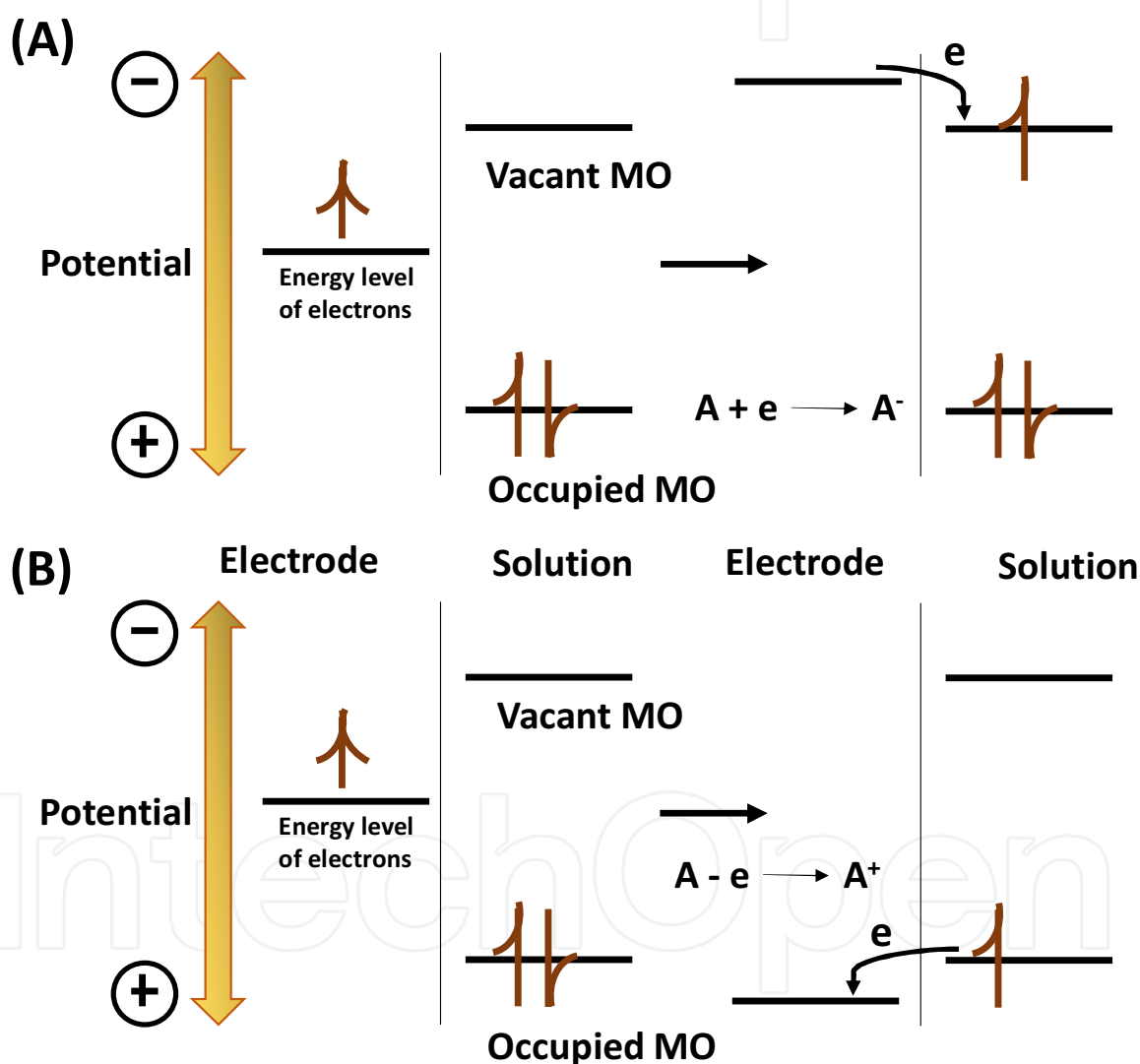

Figure 3. Representation of (A) the reduction and (B) oxidation of a species A in solution. The molecular orbitals (MO) shown for species A are the highest occupied MO and lowest vacant MO [46].

In electrolysis, by selecting the over-potential as means of adjusting the driving force for the reaction, the reaction rate of a system can be easily controlled. With increasing cathodic potential, the concentration of the electrochemical active species, reacting at the cathode, is

increasingly reduced in the immediate vicinity of the electrode until every incoming ion is directly reduced. The reaction becomes limited by mass transport processes arising from the depletion of cations in the diffusion layer. The current stays constant even if the over-potential is further increased. This current, limited by diffusion, is denoted diffusion threshold current I_d. In the case of convection, the diffusion layer is of constant thickness δ (stationary case). Mass transport can be described by Fick's first law of diffusion, and the limiting current I_d (at an electrode with the area A) only depends on the bulk electrolyte concentration c_0:

$$I_d = nFAD\frac{c_0}{\delta} \tag{4}$$

The advantages of electrodeposition technique over physical deposition methods are as follows: no need of vacuum equipment, easier handling, higher deposition rates and easier to prepare thick and continuous films. The metal deposition operation depends on a great number of chemical and operational parameters such as local current density, electrolyte concentrations, complexing agents, buffer capacity, pH, levelling agents, brighteners, surfactants, contaminants, temperature, agitation, substrate properties, cleaning procedure. All these parameters act on the structure of the deposit and also on its composition, in terms of alloy and its properties. Accordingly, the determination of these parameters is very important.

Generally, a given metal is electrodeposited from a cell consisting two conductive electrodes, a reference electrode to maintain the potential between the conductive electrodes, an electrolyte and a power supply for conducting an electrical current through the cell or applying an external electric field in the electrolyte. As the current flows into the cell, an oxidation reaction occurs on one electrode (called anode) by charging growth species (typically positively charged metal ions) into the electrolyte and consequently a reduction reaction takes place on the other electrode (called cathode), reducing the charged growth species at the growth or deposition surface as a metallic layer. The process can be carried out using potentiostatic or galvanostatic deposition, depending upon whether applied potential or current is adjusted precisely for the given material to be deposited.

In order to get a qualitative interpretation of the different processes that occur at an electrode, a cyclic voltammogram can be a very helpful tool. The basic idea is that a potential sweep is applied from one to another potential and vice versa with a certain constant speed (mV/s), resulting in a potential triangle (sawtooth) in time (Fig. 4(A)). Because the sign of the potential is changed, oxidative and reductive processes can be distinguished. In addition, varying the scan rate, i.e. triangle slope, different processes at the electrode can be measured. Figure 4 shows the triangle slope and the current flowing through the cathode as function of applied potential.

A similar method has been frequently used for electrodeposition of magnetic nanowires into nanoporous membranes. A metal layer like Au is deposited on one side of the template to provide electrical contact which serves as working electrode, a platinum strip as counter electrode and a saturated calomel electrode (SCE) as a reference electrode. Figure 5(A)
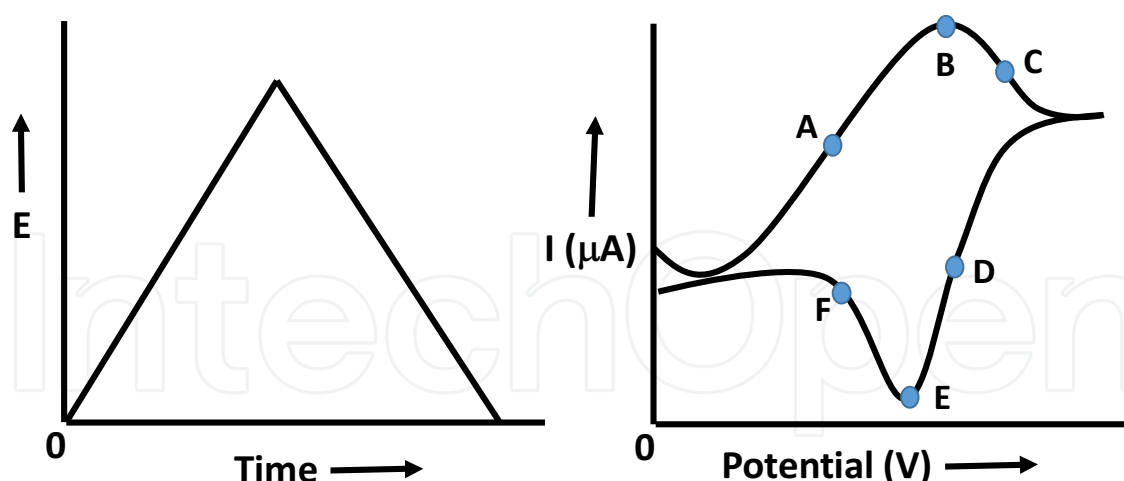
Figure 4. A triangular-shaped potential scan and the resulting current response at a stagnant electrode.

illustrates the common set-up for the template-based growth of nanowires using electrode-position. Chronoamperometry of nanowire deposition is shown in Fig. 5(B). A pre-growth stage occurs when a sudden drop of current takes place once the potential is applied through the cell during which nucleation starts at the pore bottoms. Consequently, a slightly increased current is observed at which the metal is growing in the pores. As pores are filled, current decreases with a large gradient versus time. At the final step, hemispherical caps, originating from each nanowire, form a coherent planar layer that expanded to cover the whole surface of the template. Thus, the effective cathode area increases and a rapidly increasing deposition current can be observed.
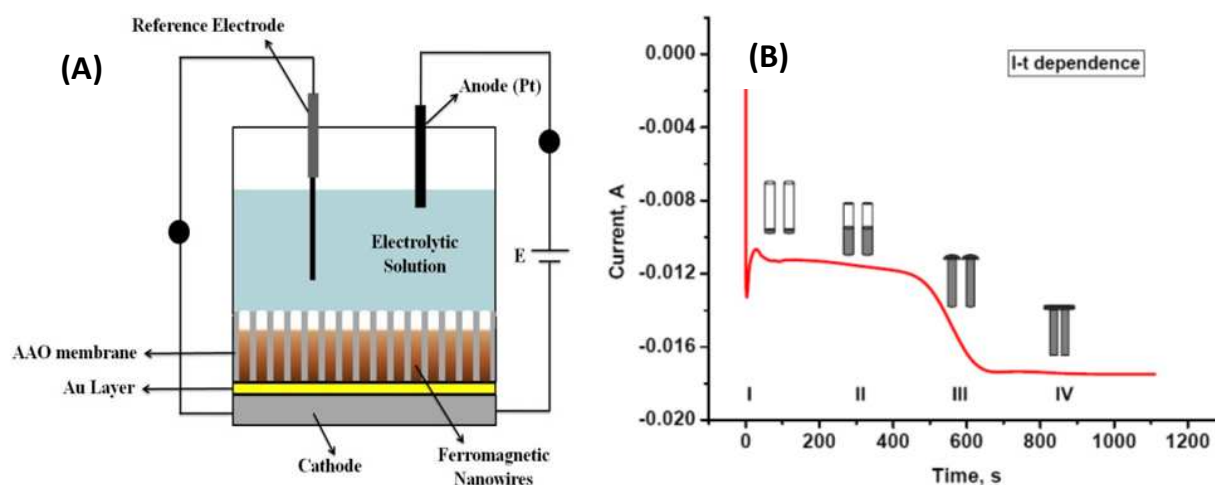

Figure 5. (A) Schematic of electrochemical cell used for nanostructure synthesis. (B) Typlical chronoamperommetry plot during electrodeposition.

For nanotube growth in AAO, instead of a thick Au layer, a very thin layer of Au <30 nm was sputtered on one side of AAO template, so as not to completely block bottom of the pores as
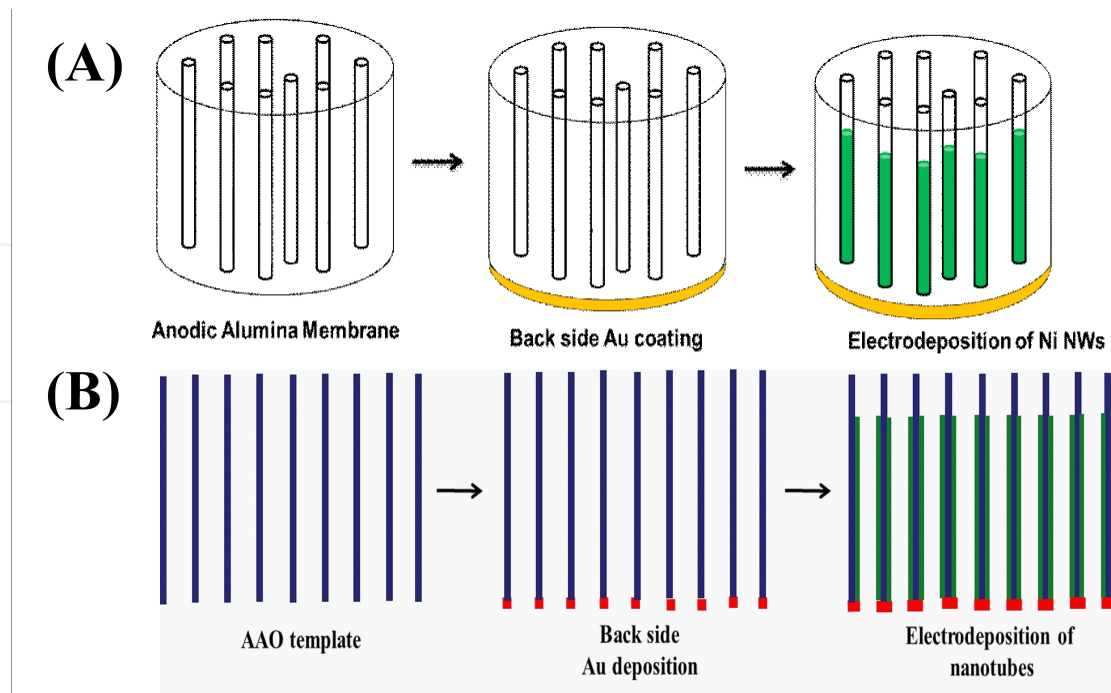
Figure 6. Steps followed for depositing (A) nanowires and (B) nanotubes in AAO template.

shown in Fig. 6(B). Nanotubes (NTs) wall thickness depends upon back-side Au layer as when Ni ion moves to the pores of the template under the drive of electric field, Ni ion firstly reaches the conducting Au layer of the pore-mouth and is deoxidized Ni atom, and thus forms a tubular structure. The wall thickness of nanotubes also depends upon other factors like the current density; therefore, we choose deposition potential in such a manner to achieve low current density. A special attention is paid to address a comparative analysis of the careful preparation of Ni NW (nanowire) and NT (nanotube) arrays with well-controlled ordering and their structural and magnetic response. Table 1 shows the previous research work on ferromagnetic nanowires and nanotubes for various deposition parameters.

Composition	Deposition Potential (V)	pH	Reference
Ni NWs	-1.1 to -1.5	3.5	[36-38]
Co NWs	-1.0	3-5	[38, 39]
$Ni_{80}Fe_{20}$ NWs	-1.2 to -1.4	3	[40]
Ni NTs	-0.2 to -1.5	2-3	[13-15]

Table 1. Electrolytic deposition parameters of various ferromagnetic nanowires and nanotubes.

Electrolytic bath for the deposition of specific ferromagnetic material was prepared using their corresponding sulphate salts; boric acid was added in each bath solution to prevent hydroxide formation and promoting deposition rate. Table 2 describes the electrolytic bath concentrations and electrodeposition parameters used for various nanowires and nanotubes deposited.

Composition	Electrolytes Used	Molar Weight/100 ml	Deposition Potential (V)	pH
Ni NWs	$NiSO_4$, $NiCl_2$, H_3BO_3	33 g, 4.5 g, 3.8 g	-1.0	2.5
Co NWs	$CoSO_4$, H_3BO_3	12 g, 4.5 g	-1.3	3.5
$Ni_{60}Fe_{40}$ NWs	$NiSO_4$, $FeSO_4$, H_3BO_3	12 g, 0.6 g, 4 g	-1.2	3
$Co_{75}Fe_{15}B_{10}$ NWs	$CoSO_4$, $FeSO_4$, H_3BO_3, DMAB	4.95 g, 0.834 g, 4.33 g, 0.049 g	-1.2	2
Ni NTs	$NiSO_4$, PEG, H_3BO_3	1.5 g, 3.7 g, 3.5 g	-0.7	2

Table 2. Electrolytic concentration and deposition parameters of various ferromagnetic nanowires.

The deposition potential of the electrolyte bath with respect to the reference electrode SCE is determined by cyclic voltammetry. Figure 7 shows the typical voltammogram for the Ni, Co, NiFe alloy and CoFeB amorphous nanowires used in this chapter. Typically, the potential is chosen at a reducing potential where current starts decreasing. For the growth of the NWs/NTs chrono-amperommetry is used at various deposition times which controls the length of the nanostructures. The wall thickness of nanotubes also depends upon the current density; therefore, we choose deposition potential in such a manner so as to achieve low current density [37].
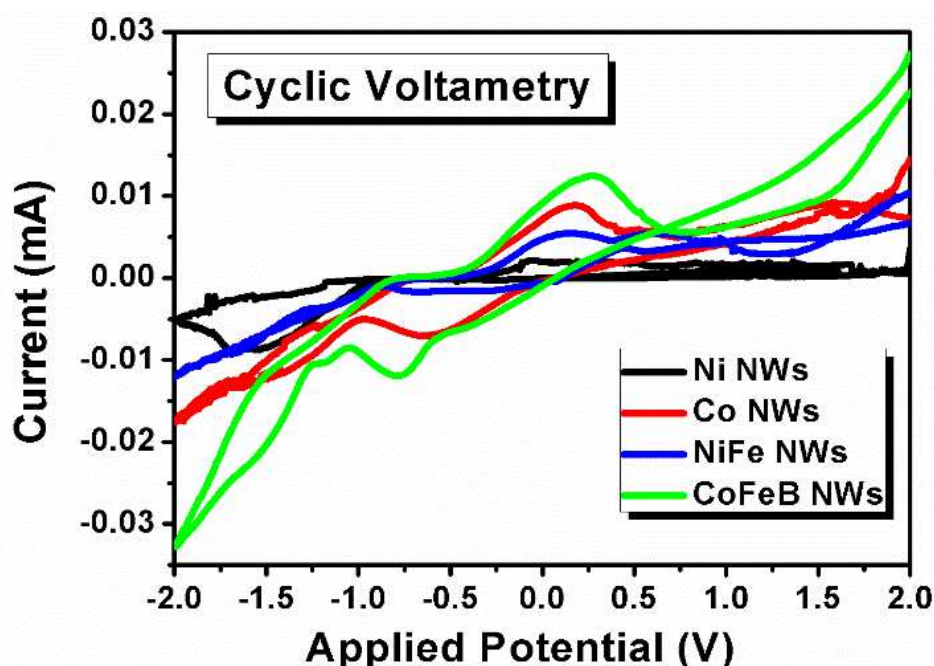

Figure 7. Cyclic voltammogram of various electrolyte baths for determination of deposition potential taken at a sweep of 2 mV/sec.

4. Characterization

In this section, various characterization techniques are discussed to determine the physical and magnetic properties of electrodeposited nanostructures. The morphology and size of nanostructures were characterized by scanning electron microscope (SEM). The qualitative and quantitative elemental composition of nanostructures were done using energy dispersive X-ray analysis (EDX). The structural analysis of ferromagnetic nanowires and nanotubes was done by transmission electron microscope (TEM) and X-ray diffraction (XRD) spectroscopy. Magnetic properties of the samples were tested by superconducting quantum interference device (SQUID).

The morphology of the NWs/NTs was observed by dissolving the template in 3M NaOH solution for 1 h. The separated nanostructures were cleaned several times with de-ionized water and mounted on holder for SEM. Figure 8 (A-D) shows the SEM images of nanowires which revealed that most nanochannels of AAO template are highly filled and parallel to each other. The nanowires have continuous structure without visible defects replicating the pore shapes. It means that ferromagnetic material fills the pores uniformly during electrodeposition under controlled conditions used in this work. Cross-sectional SEM images were taken simply by cleaving of alumina templates. Figure 9 (A-B) shows the SEM images of Ni nanotubes revealing that the wall thickness is around 40 nm and it strongly depends upon the back-side coating of metallic layer.

For EDX analysis, we mounted the nanowire's deposited sample on SEM holder and coated them with carbon since the absorption of X-ray signal by carbon coating is negligible on account of its low atomic number and is taken into account while performing quantitative EDX analysis. Figure 10(A-D) shows the EDX spectrum for various nanowires of Ni, Co, CoFeB and NiFe alloy, confirming the presence of respective elements in the AAO template. The quantitative analysis for CoFeB nanowires determines the stoichiometry of composite material such as $Co_{75}Fe_{15}B_{10}$ and for NiFe alloy such as $Ni_{60}Fe_{40}$.

For TEM characterization, the specimen was obtained by completely dissolving the AAO template in 3M NaOH solution for 24 h and then washing with de-ionized water several times. The free NWs/NTs were then collected from the suspension by applying a magnetic field using a permanent magnet and then rinsed with ethanol and immersed in an ultrasonic bath for 10 min. When operated in the diffraction mode, TEM images also yield information regarding the crystal structure of the nanostructure axis by selected area electron diffraction pattern (SAED).

Figure 11(A-B) shows the TEM image of Co and CoFeB NWs. Figure 12 shows diffraction pattern of the nanowires which revealed the single crystal phase for Co nanowires while the SAED pattern for CoFeB nanowires shows the amorphous phase. TEM images of Ni nanotubes are shown in Fig. 13(A) with inner and outer diameters of about 120 nm and 200 nm. It also confirms that the wall thickness of nanotubes is ~40 nm as observed in the SEM images. The branching due to AAO templates causes the growth of nanotubes in Y-shape nanochannels as observed in Fig. 13(B).
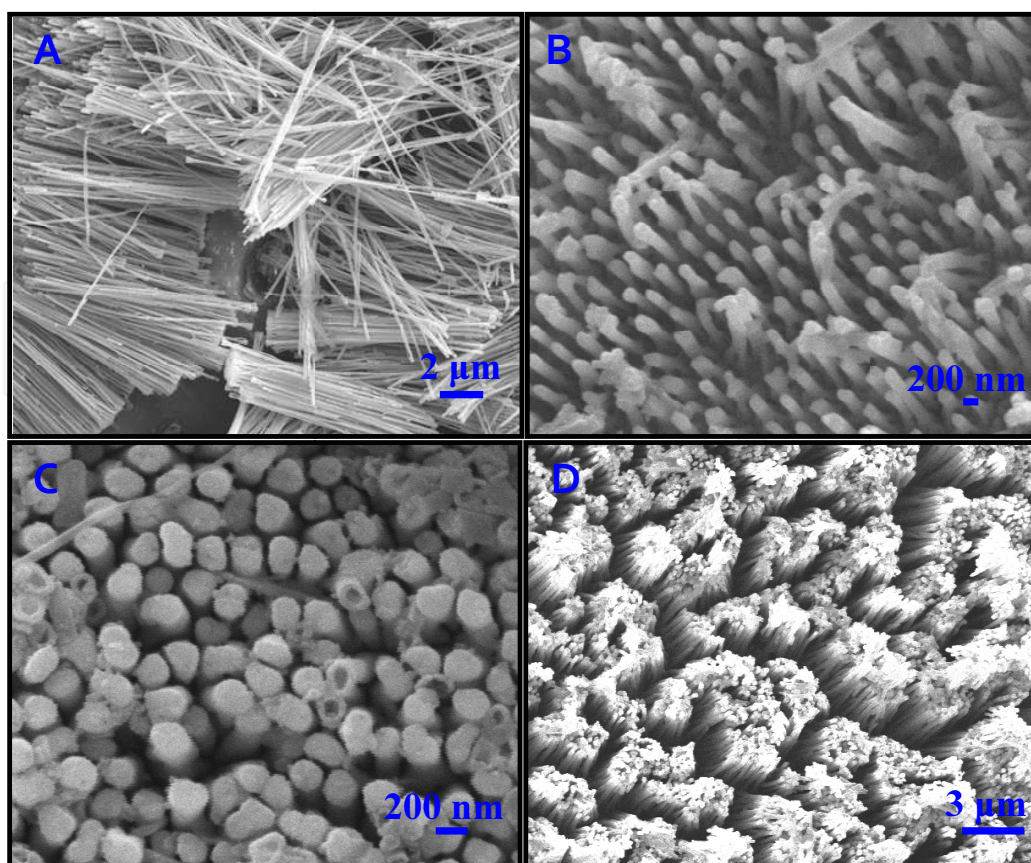
Figure 8. (A-D) shows the top and cross-sectional view of AAO templates before and after the deposition of nanowires. The images confirmed that the diameter of the nanowires are ~200 nm and the interwire spacing between the pores is ~300 nm.
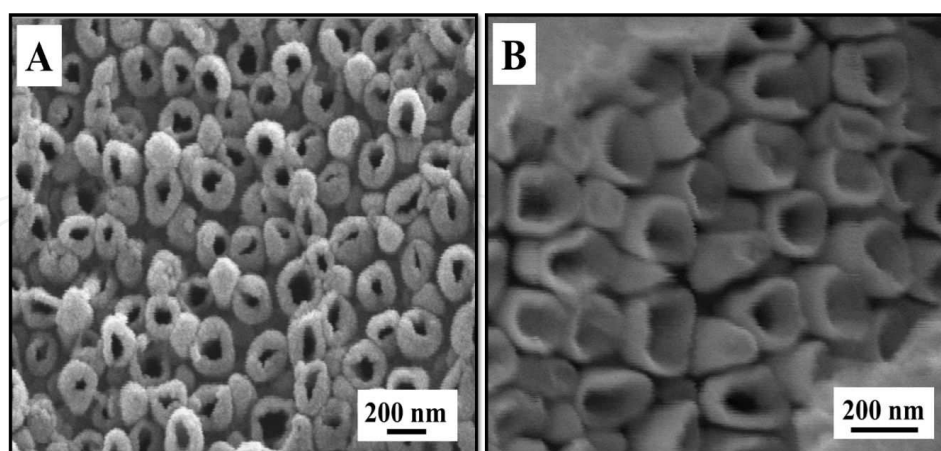

Figure 9. (A-B) SEM images of Ni nanotubes embedded in AAO template with wall thickness of 40 nm.

For determining the crystallographic information of the materials, XRD is one of the most important technique. It can provide information about the crystallographic phases, crystallite size, lattice constant, presence of impurities, etc. X-ray diffraction was performed using Philip's
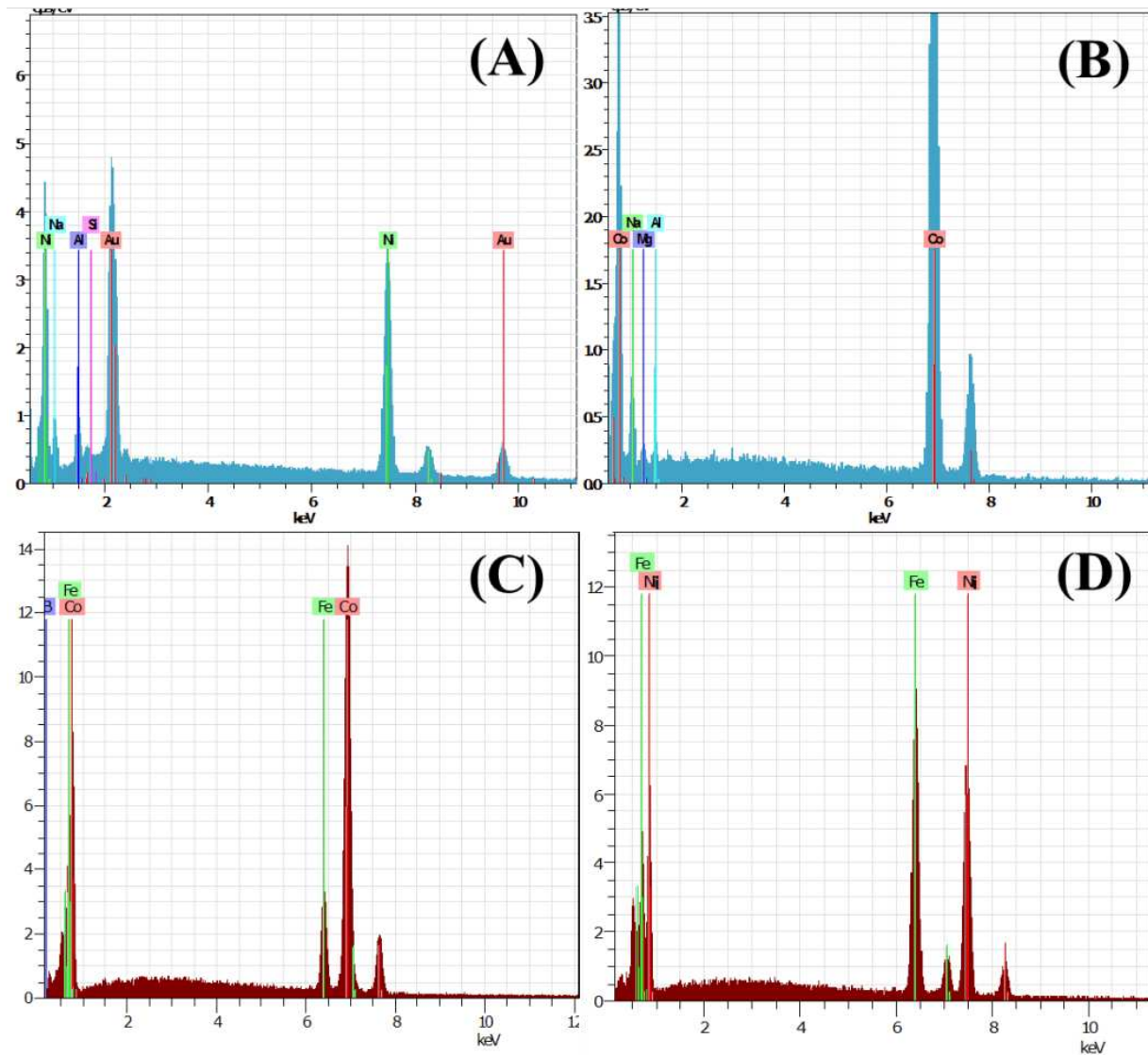
Figure 10. EDX spectra of various nanowires deposited in AAO template (A) for Ni, (B) for Co, (C) for CoFeB, and (D) NiFe alloy.

X'pert PRO (Model PW 3040, X-ray wavelength of Cu Kα line λ = 1.54060 Å) diffractometer. The phase was identified using standard diffraction files of JCPDS. The size of the crystalline material can be estimated from the width of the reflection plane using Scherer equation [41]:

$$D_{crystalline} = \frac{\kappa\lambda}{\beta cos\theta}$$

(5)

where κ is a particle shape factor (for spherical particles, κ=0.9, β is the full width at half maximum (radians) and $D_{crystalline}$ is diameter of the crystallites (Å). It is useful to eliminate the instrumental line width from the observed one to get a correct broadening value due to small particle size.
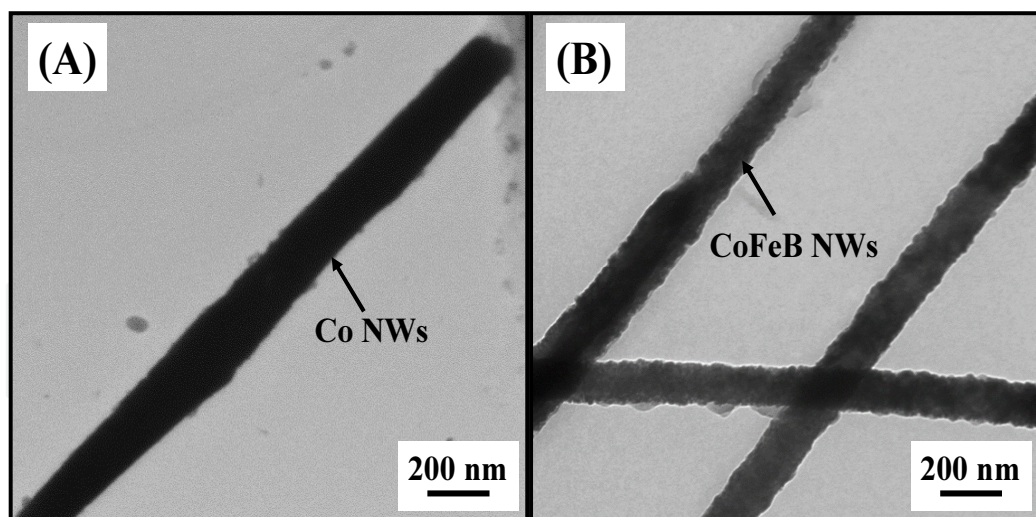
Figure 11. (A-B) TEM morphologies of Co and $Co_{75}Fe_{15}B_{10}$ nanowires with pore diameter of 200 nm.

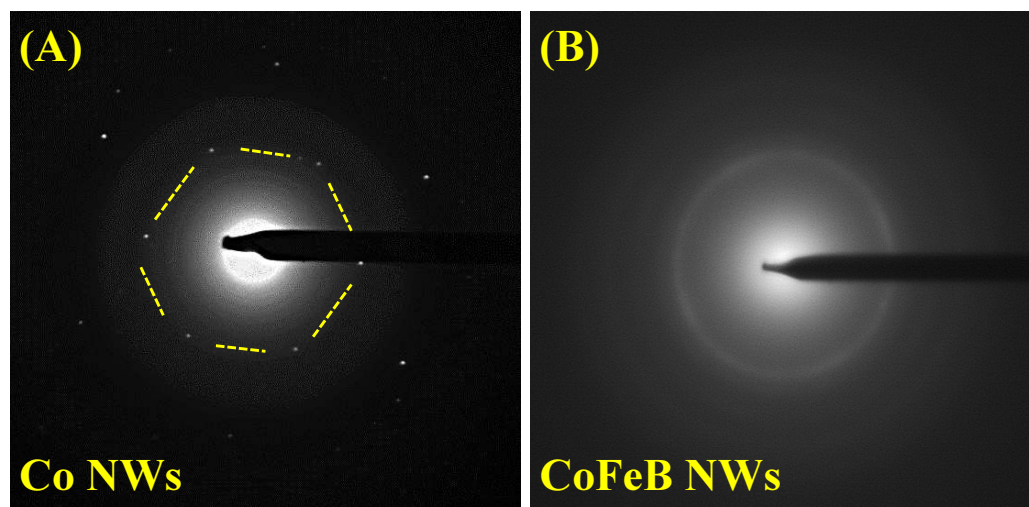**Figure 12.** SAED pattern of (A) a single crystal Co nanowire having hcp structure and (B) amorphous phase of $Co_{75}Fe_{15}B_{10}$ nanowires. Dotted lines are guidelines to eye.

Figure 14 shows the XRD pattern of various ferromagnetic nanowires grown in anodic alumina templates by electrodeposition method. The spectra for the nanowires indicates polycrystalline reflection peaks. The diffraction peaks confirms the *fcc* lattice structure in all deposited nanowires except for CoFeB nanowires. The only intense broad peak of CoFeB nanowires is due to a small bcc CoFe (110) phase, which occurs if the content of Fe is less. The diffracto-gram indicates that CoFeB nanowires appears in the amorphous phase. We compare the XRD spectra of Ni nanowires and nanotubes as shown in Fig. 15. XRD measurements illustrate a face-centred cubic (*fcc*) Ni pattern for NWs and NTs in AAO templates. Compared to the peak positions of standard Ni (JCPDS, 04-0850), peaks are found to be in agreement with peak positions of Ni ((111), (200), (220)).
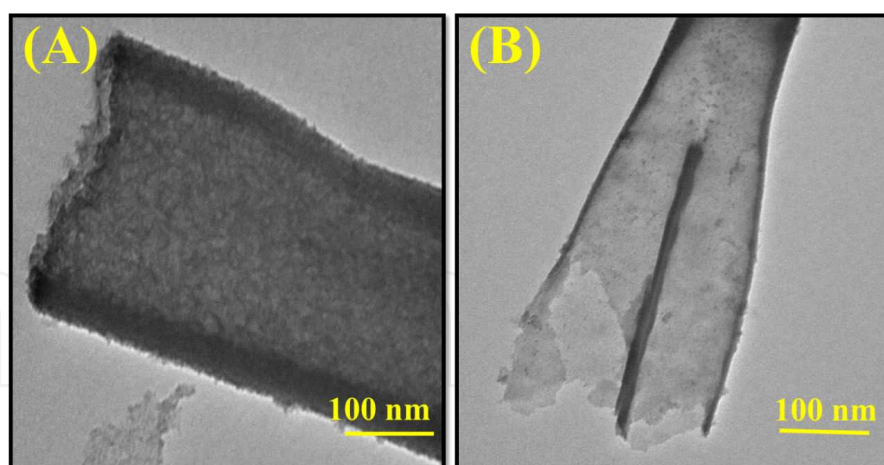
Figure 13. (A) TEM image of isolated Ni nanotube, (B) Y-shape growth of nanotube caused by the branching of AAO templates.
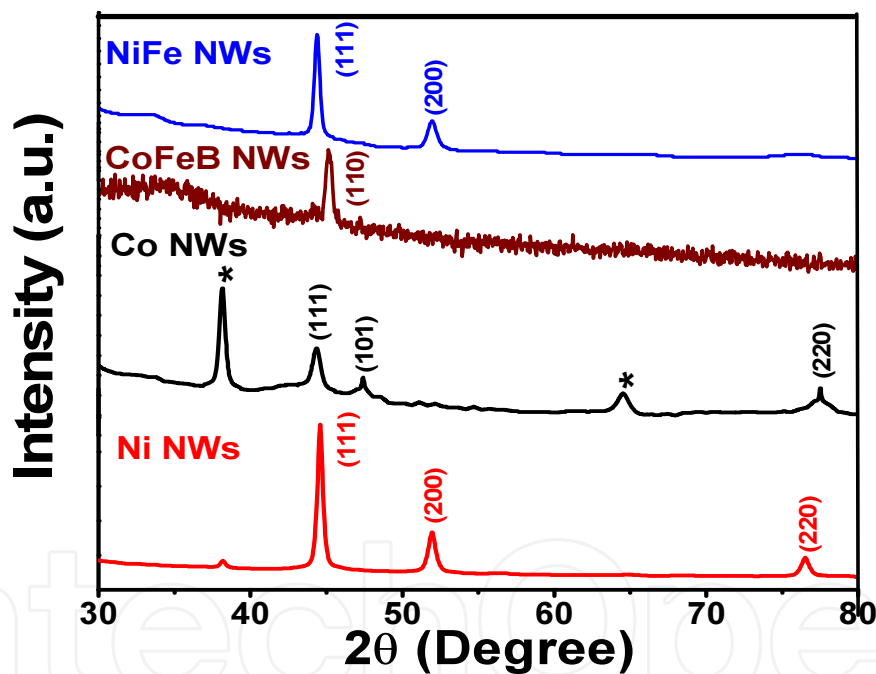

Figure 14. X-ray diffraction pattern of ferromagnetic nanowires electrodeposited in AAO templates. The * peaks in the XRD pattern of Co NWs are due to the Au layer on back side of the template.

The NWs and NTs were found strongly textured along (111) reflection plane. The crystallite size of the deposited nanostructures was determined using Scherrer formula, giving 22 nm and 16 nm for NWs and NTs, respectively. This is due to the fact that their outer diameter is the same, ~200 nm, but NTs have a core cylindrical hole with an estimated diameter of 120 nm. The corresponding d-spacing was observed to be 2.04 nm and 2.03 nm for NWs and NTs, respectively. We also determined the crystallite size of all these nanostructures as given in Table 3.

Material	Peak Position 2θ (Degree)	FWHM β (Degree)	Crystallite Size (nm)	d-spacing (nm)
Ni NWs	44.33	0.42	22.0	2.04
Ni NTs	44.52	0.56	16.4	2.03
Co NWs	44.35	0.63	14.7	2.04
$Ni_{60}Fe_{40}$ NWs	44.41	0.48	19.3	2.04

Table 3. XRD peak positions, FWHM, crystallite size and d-spacing of various nanostructures.
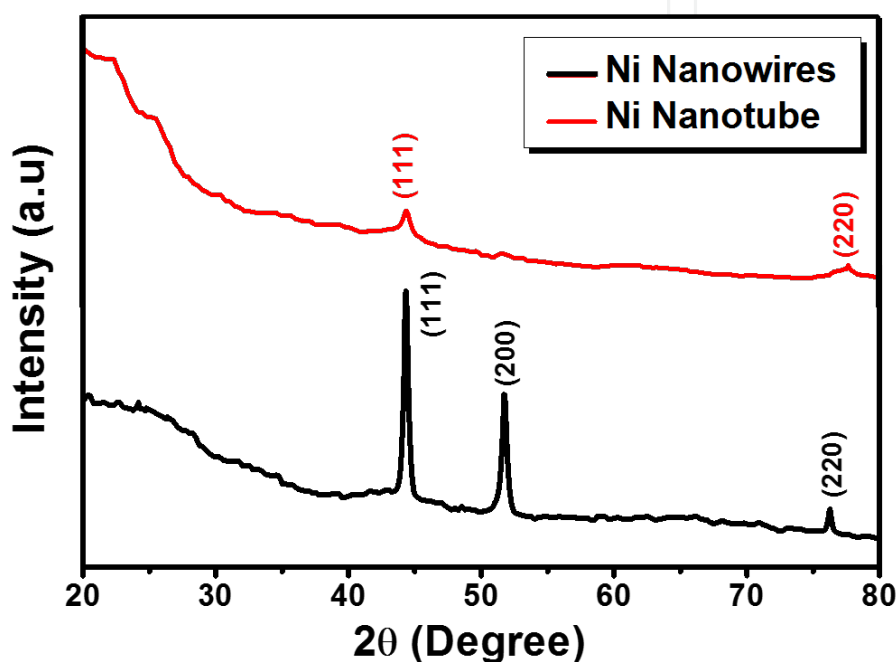

Figure 15. XRD spectra of Ni nanowires and nanotubes electrodeposited in AAO templates.

The hysteresis loops were measured in two geometries: when the applied magnetic field H is perpendicular to wire's axis and also parallel to wire's axis. The orientation of NWs and NTs embedded in AAO with applied external magnetic field in SQUID was ensured during sample preparation. For parallel and perpendicular arrangement, the templates were fixed in a small piece of folded straw which is further inserted in a new straw in such a way that it is along the easy and hard axis of straw elongation. An analysis of hysteresis loops allowed us to determine the values of coercivity (H_c) and normalized remanent magnetization (M_r). The saturation magnetization M_s value has been taken from reported works [42]. Figure 16 shows the hysteresis loop of typical Ni NWs having length 30 μm with the applied magnetic field parallel and perpendicular to the long axes of the nanowires. The difference between the hysteresis loops for the two orientations suggests the existence of magnetic anisotropy in the sample. The Ni NWs are not exactly uniform from the bottom to the top of the nanowires due to the Y-shaped templates being used. Y-shaped portion (Fig. 2) has a different shape anisotropy and

dominates in magnetostatic coupling than the long-portion. This can only be seen as an averaged, smoothed curve in the SQUID measurements. Due to averaging, the easy axis loops show a curved shape and a consequent reduction in the squareness. The values of remanent magnetization $M_r(||)$ and $M_r(\perp)$ for 30 μm sample are 0.26 memu and 0.072 memu, respectively. This indicates that the magnetic easy axis of the system is along the axis parallel to the nanowires. The squareness (M_r/M_s) of the hysteresis curve is greater when the applied field is parallel to the nanowires than perpendicular to it. The values of coercivity $H_c(||)$ and $H_c()$ for 30 μm sample are 124 Oe and 84 Oe, respectively.
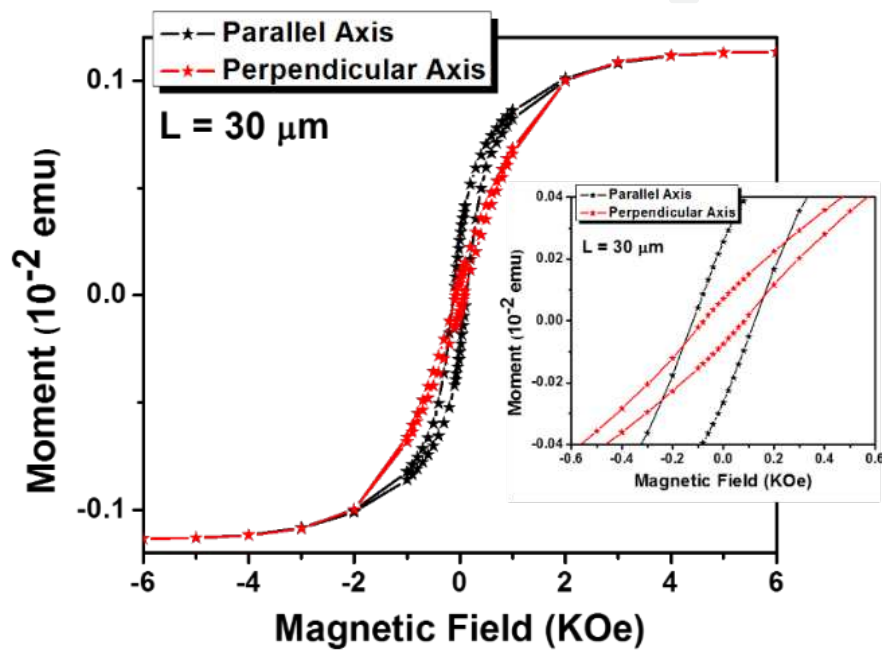

Figure 16. Magnetization loops for Ni NWs of length 30 μm at different orientation of the applied magnetic field at room temperature.

Figure 17 shows the magnetic hysteresis loop of Ni nanotube. The nanocylinders geometry, i.e. their length, inner and outer radii (R_{in} and R_{out}) and wall thickness (t_w) strongly affects the magnetization reversal mechanism. In our work also, we observed a magnetization reversal switching in nanotube geometry. One can easily observe that for nanowires (Fig. 16), the easy axis is along the wire's long axis, whereas for nanotubes (Fig. 17), the easy axis is parallel to the tube axis resulting in a magnetization switching. Since the deposited nanostructures have an *fcc* structure, which shows small magneto-crystalline anisotropy, magnetic anisotropy is mainly decided by the competition between the shape anisotropy of the individual NW/NT and the magnetostatic interaction between neighbouring NWs/NTs.

The values of coercivity $H_c(||)$ and $H_c(\perp)$ for NTs are 32 Oe and 41 Oe, respectively. Both curves are highly sheared, indicating strong inter-tubular interaction. Further, it is clear from the evidence that the array has very low remanence magnetization. The values of remanent
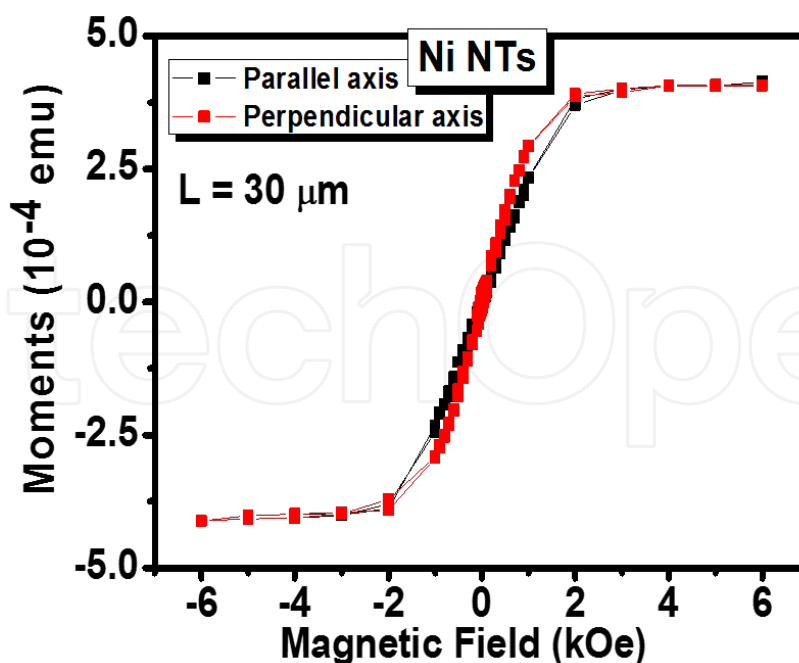
Figure 17. Magnetization loops for Ni NTs of length 30 μm at different orientation of the applied magnetic field at room temperature.

magnetization $M_r(||)$ and $M_r(\perp)$ for 30 μm Ni NT sample are 0.006 memu and 0.017 memu, respectively. The remanent magnetization of Ni NTs is very small as compared to NWs, which is due to less volume of magnetic material present in nanotubes (hollow inside).

5. High-frequency applications

Investigations on the magnetization reversal modes of Ni NWs/NTs are done by angular-dependent FMR measurements. Here we will discuss the quantitative analysis of resonance frequency (*f*) and frequency line-widths (Δ*f*) data. Depending upon the geometry of the nanostructures, basically three main modes of magnetization reversal exist: *coherent mode* (C), where all spins rotate homogenously; *vortex mode* (V), in which vortex-like domain wall nucleates and propagates; *transverse mode* (T), in which spins rotate progressively via propagation of a transverse domain wall.

Figure 18(A-D) shows the transmission response for arrays of Ni NWs and NTs used in the present study. In order to view the effect of interactions between NWs/NTs of FMR spectra, the resonance frequency and frequency line-width as a function of applied field was observed. Resonance frequency increases linearly with the increase of external magnetic field for all four samples. The magnetic bias field was rotated from parallel orientation of nanostructures to that of perpendicular to them for angular variation measurements. The resonance frequency ($f_r = \omega/2\pi$) as a function of field orientation can be obtained from Landau–Lifshitz–Gilbert equation as [21, 26]:

$$\left(\frac{\omega}{\gamma}\right)^2 = \left[Hcos\left(\theta - \theta_H\right) + H_{eff}cos^2\theta\right]\left[Hcos\left(\theta - \theta_H\right) + H_{eff}cos2\theta\right] \qquad (6)$$

where $\omega = 2\pi f$ and $\gamma = g\mu_B/\hbar$ is the gyromagnetic ratio, θ_0 is the angle between magnetization equilibrium direction and easy axis, and θ_H is the applied field direction measured from the easy axis. At the resonance frequency $\omega = \omega_r$, $\theta = \theta_H$ and the applied field $H = H_{res}$ in the saturated case.
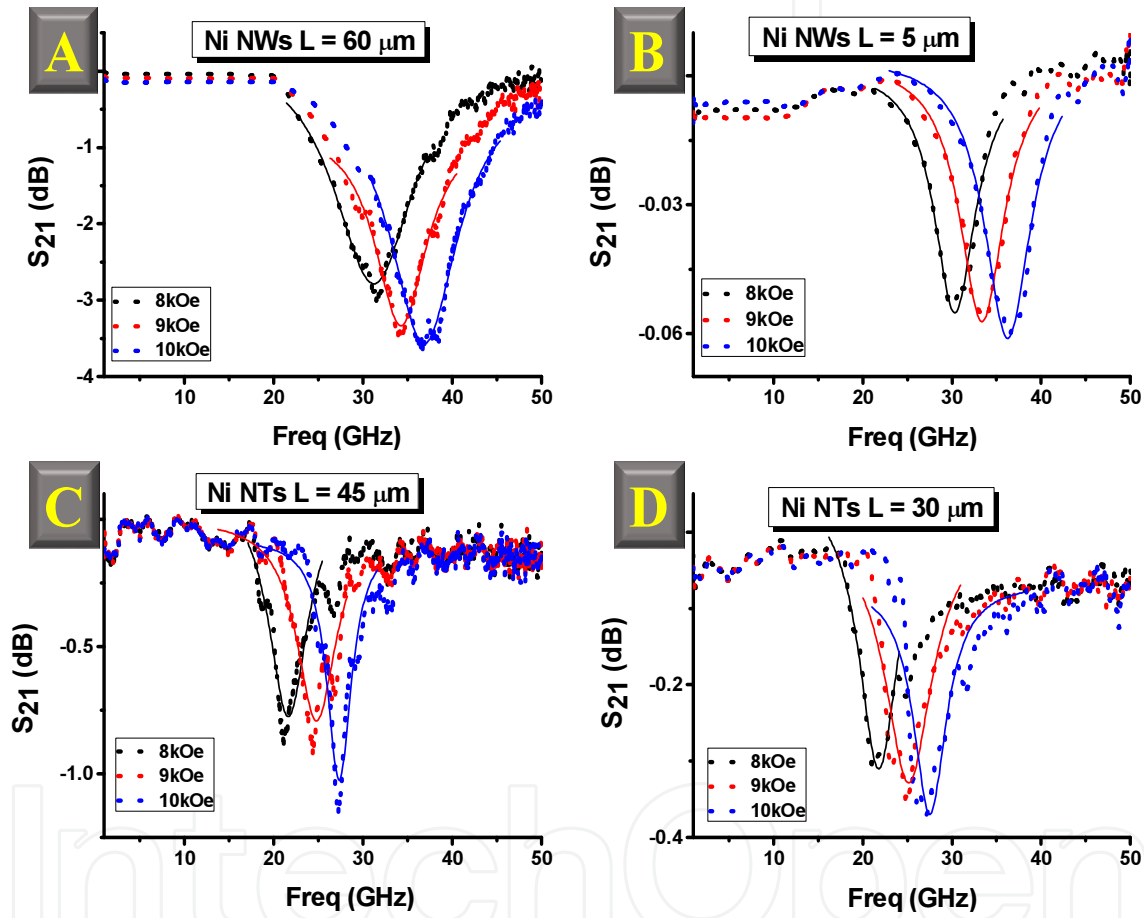

Figure 18. (A-D). Experimental transmission response (S_{21} vs. frequency) at different applied fields along parallel orientation of long axis of ferromagnetic nanowires and nanotubes of diameter 200 nm and various lengths. Solid lines are the Lorentzian fits to the experimental data.

The angular dependence of f_r for NWs and NTs is shown in Fig. 19(A). NW array exhibits stronger magnetic interaction than the NT arrays. In nanotubes, there is a transition in magnetization reversal mode at very small tube radius. The curling mode of magnetization reversal in an infinite cylinder predicts that f_r increases as angle (θ_H) increases from 0° to 90°, whereas coherent rotation mode gives highest and lowest f_r values for $\theta_H = 0°$ and $\theta_H = 90°$, respectively.

Figure 19(B) shows the theoretical results for angular dependence of f_r for NW and NT arrays. The results were calculated using Eq. (6) for the uniform mode and the corresponding equilibrium conditions. In a nanowire array, each nanowire is exposed to the field created by the neighbouring wires in addition to the self-demagnetizing field and hence the demagnetization field is given as $H_d = 2\pi M_s$ (1-3P), where P is the volume fraction of the magnetic nanostructure in the matrix. In case of nanotubes, the demagnetization field is no longer similar to that of the nanowires. Also, it is assumed that the nanotubes do not have the extreme surfaces as seen in wires to give rise to an additional interaction field that would oppose the tubes' shape anisotropy. It is also found that the magnetic anisotropy is sensitive to the demagnetization factor, demonstrating that the magnetostatic interaction between nanotubes is responsible for the wall-thickness-dependent magnetic anisotropy [43].

With this consideration, the demagnetization factors used to calculate H_{eff} for nanotubes are given as [44]:

$$N = \frac{1}{2}\left[1 - \lambda^2\left(\frac{\mu_r - 1}{\mu_r + 1}\right)\right] \qquad (7)$$

where μ_r is the relative permeability and $\lambda = R_{in}/R_{out}$, where R_{in} is the inner and R_{out} is the outer radii of the nanotube, respectively. In our case λ is found to be 0.6.
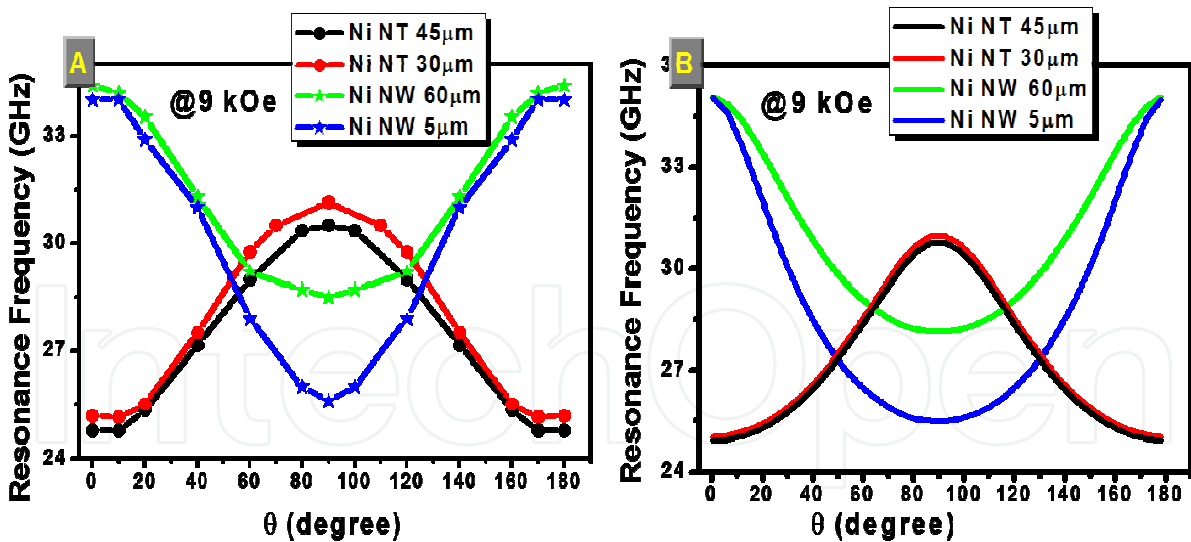

Figure 19. (A) Angular variation of the FMR frequency positions ($f_r(\theta_H)$) measured at an applied field of 9 kOe, (B) theoretical curves fitted from Eq. (6). $\theta_H = 0°$ corresponds to the applied magnetic field parallel to the NWs/NTs axis and $\theta_H = 90°$ corresponds to perpendicular configuration.

The bell-shaped f_r curves in Fig. 19(A) clearly shows a negative effective field for the nanotubes with the easy plane perpendicular to the nanotubes. At the parallel (low and high extreme values of θ_H) and perpendicular conditions there is a good agreement between the theoretical

and experimental f_r value for both nanotubes and nanowires, while in the range of $\theta_H = 40°$-$80°$ and corresponding angles in the next quadrant, there is a difference in the f_r values. This difference can be attributed to the situation where the spins in the nanostructures under consideration vary spatially and hence the effective field cannot explain the mean magnetization in a particular direction giving rise to the coherent uniform rotation. This reveals the inhomogeneous internal and stray field in the NWs and NTs of small radii, which needs further investigation.
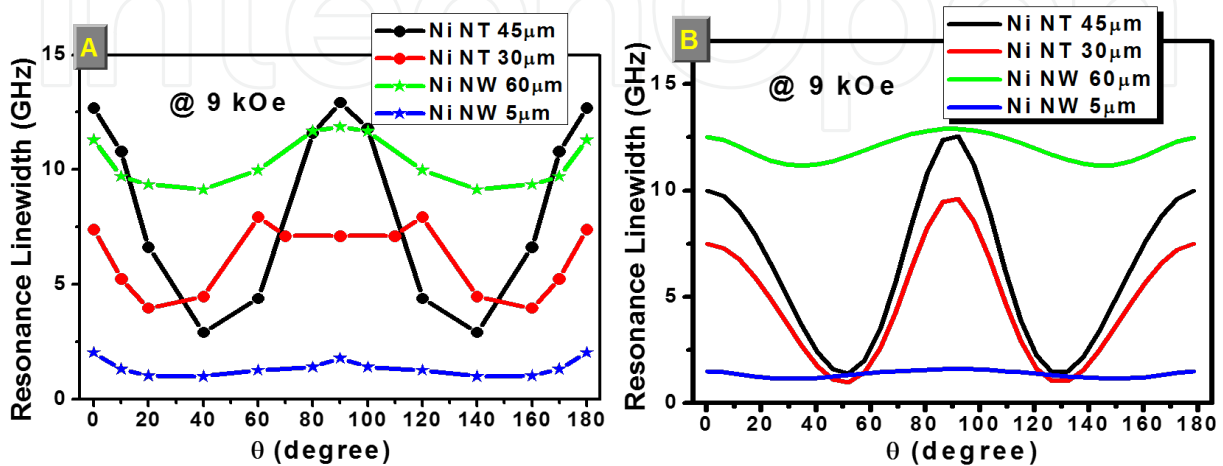

Figure 20. (A) Angular variation of FMR line-widths (Δf) measured for all samples at an applied magnetic field of 9 kOe, (B) theoretical curves fitted from Eq. (8).

Figure 20(A) shows the FMR line-width (Δf) as a function of θ_H for all samples. Δf was determined from the Lorentzian fit to the transmitted signal from the sample. The line-width reflects the distribution of the parameters of individual nanostructures that vary in their exact orientation inside the template as well as in their value of effective anisotropy field. Theoretical curves showing the angular dependence of frequency line-width is shown in Fig. 20(B). The frequency line-width is found using the following relation:

$$\Delta\left(\frac{\omega}{\gamma}\right) = \left(\frac{d(\omega/\gamma)}{dH}\right)\Delta H(\theta_H) \qquad (8)$$

where ΔH is given by [45]

$$\Delta H = \Delta H_0 + 1.16\alpha\left(\frac{\omega}{\gamma}\right) \qquad (9)$$

ΔH_0 is the frequency independent contribution to the line-width caused by inhomogeneous broadening. It is found that the shape of the line-width curves is similar in both experiment and theory.

These studies show that ferromagnetic nanostructures embedded in AAO templates fabricated by electrodeposition technique are the best candidates for high-frequency application devices.

Author details

Monika Sharma[1*] and Bijoy K. Kuanr[2]

*Address all correspondence to: monikasharma1604@gmail.com

1 Indian Institute of Technology Delhi, New Delhi, India

2 Special Centre for Nanoscience, Jawaharlal Nehru University, New Delhi, India

References

[1] F. Byrne, A. Prino-Mello, A. Whelan, B. M. Mohamed, A. Davis, Y. K. Gunko, J. M. D. Coey, and Y. Volkov, "High content analysis of the biocompatibility of nickel nanowires," *J Magn Magn Mater*. 321 (2009), pp. 1341-1345.

[2] A. A. Stashkevich, Y. Roussigne, P. Djemia, S. M. Cherif, P. R. Evans, A. P. Murphy, W. R. Hendren, R. Atkinson, R. J. Pollard, A. V. Zayats, G. Chaboussant, and F. Ott, "Spin-wave modes in Ni nanorod arrays studied by Brillouin light scattering," *Phys Rev B*. 80 (2009), pp. 144406.

[3] D. V. Berkov, C. T. Boone and I. N. Krivorotov, "Micromagnetic simulations of magnetization dynamics in a nanowire induced by a spin-polarized current injected via a point contact," *Phys Rev B*. 83 (2011), pp. 054420.

[4] S. F. Chen, H. H. Wei, C. P. Liu, C. Y. Hsu, and J. C. A. Huang, "Microstructural effects on the magnetic and magnetic-transport properties of electrodeposited Ni nanowire arrays," *Nanotechnology*. 21 (2010), pp. 425602.

[5] A. N. Banerjee, S. Qian, and S. W. Joo, "Large field enhancement at electrochemically grown quasi-1D Ni nanostructures with low-threshold cold-field electron emission," *Nanotechnology*. 22 (2011), pp. 035702.

[6] X. Kou, X. Fan, R. K. Dumas, Q. Lu, Y. Zhang, H. Zhu, X. Zhang, K. Liu and J. Q. Xiao, "Memory effects in magnetic nanowire arrays", *Adv Mater*. 23 (2011), pp. 1393-1397.

[7] Y. Xia, P. Yang, Y. Sun, Y. Wu, Y. Yin, F. Kim, and H. Yan, "One-dimensional nanostructures: Synthesis, characterization and applications," *Adv Mater*. 15 (2003), pp. 353-389.

[8]   Y. C. Sui, R. Skomski, K. D. Sorge, and D. J. Sellmyera, *Appl Phys Lett*. 84 (2004), pp. 1525.

[9]   X. Duan, and C.M. Lieber, "General synthesis of compound semiconductor nano-wires," *Adv Mater*. 12(2000), pp. 298–302.

[10] T. M. Whitney, J. S. Jiang, P. C. Searson, and C. L. Chien, "Fabrication and magnetic properties of arrays of metallic nanowires," *Science*. 261 (1993), pp. 1316-1319.

[11] N. J. Gerein, and J. A. Haber, "Effect of ac electrodeposition conditions on the growth of high aspect ratio copper nanowires in porous aluminium oxide templates," *J Phys Chem B*. 109 (2005), pp. 17372-17385.

[12] S. Yue, Y. Zhang, and J. Du, "Preparation of anodic aluminium oxide tubular mem-branes with various geometries," *Mater Chem Phys*. 128 (2011), pp. 187-190.

[13] F. Tao, M. Guan, Y. Jiang, J. Zhu, Z. Xu, and Z. Xue, "An easy way to construct an ordered array of nickel nanotubes: the triblock-copolymer-assisted hard-template method," *Adv Mater*. 18 (2008), pp. 2161-2164.

[14] X. W. Wang, Z. H. Yuan, S. Q. Sun, Y. Q. Duan and L. J. Bie, "Electrochemically syn-thesis and magnetic properties of Ni nanotube arrays with small diameter," *Mater Chem* Phys. 112 (2008), pp. 329-332.

[15] D. H. Park, Y. B. Lee, M. Y. Cho, B. H. Kim, S. H. Lee, Y. K. Hong, J. Joo, H. C. Cheong, S. R. Lee, "Fabrication and magnetic characterization of hybrid double wal-led nanotube of ferromagnetic nickel encapsulated conducting polypyrrole," *Appl Phys Lett*. 90 (2007), pp. 093122.

[16] J. Bao, C. Tie, Z. Xu, Q. Zhou, D. Shen, and Q. Ma, "Template synthesis of an array of nickel nanotubules and its magnetic behaviour," *Adv Mater*. 13 (2001), pp. 1631-1633.

[17] J. Podbielski, F. Giesen, M. Berginski, N. Hoyer, and D. Grundler, "Spin configura-tions in nanostructured magnetic rings: From DC transport to GHz spectroscopy," *Superlattices & Microstructures*. 37 (2005), pp. 341-348.

[18] S. Sun, C. B. Murray, D. Weller, L. Folks, and A. Moser, *Science*. 287 (2000), pp. 1989.

[19] J. Escrig, M. Daub, P. Landeros, K. Nielsch, and D. Altbir, "Angular dependence of coercivity in magnetic nanotubes," *Nanotechnology*. 18 (2007), pp. 445706.

[20] A. Encinas, M. Demand, L. Vila, L. Piraux, and I. Huynen, "Tunableremanent state resonance frequency in arrays of magnetic nanowires," *Appl Phys Lett*. 81 (2002), pp. 2032.

[21] M. Sharma, B. K. Kuanr, M. Sharma and A.Basu, "Relation between static and dy-namic magnetization effects and resonance behaviour in Ni nanowire arrays," *IEEE Trans Magn*. 50 (2014), pp. 4300110.

[22] X. P. Huang, W. Han, Z. L. Shi, D. Wu, M. Wang, R. W. Peng, andN. B. Ming, "Electrodeposition of periodically nanostructured straight cobalt filament arrays, " *J Phys Chem*. C 113 (2009), pp. 1694–1697.

[23] S. Dubois, J. M. Beuken, L. Piraux, J. L. Duvail, A. Fert, J. M. George, and J. L. Maurice, *J Magn Magn Mater*. 165 (1997), pp. 30.

[24] M. Sharma, B. K. Kuanr, M. Sharma and A. Basu, "New opportunities in microwave electronics with ferromagnetic nanowires, " *J Appl Phys*. 115 (2014), pp. 17A518.

[25] L. P. Carignan, T. Kodera, A. Yelon, C. Caloz, and D. Menard, "Integrated and self-biased planar magnetic microwave circuits based on ferromagnetic nanowire substrates, " *Microwave Conf*. (2009), pp. 743-746.

[26] R. L. Marson, B. K. Kuanr, S. R. Mishra, R. E. Camley and Z. Celinski, "Nickel nanowires for planar microwave circuit applications and characterization, " *J Vac Sci Tech B*. 25 (2007), pp. 2619.

[27] A. Huczko, "Template-based synthesis of nanomaterials, " *Appl Phys A*. 70 (2000), pp. 365.

[28] N. I. Kovtyukhova, B. R. Martin, J. K. N. Mbindyo, T. E. Mallouk, M. Cabassi, and T. S. Mayer, *Mater Sci Engin C*. 19 (2002), pp. 255.

[29] R. C. Furneaux, W. R. Rigby, and A. P. Davidson, "The formation of controlled-porosity membranes from anodically oxidized aluminium, " *Nature*. 337 (1989), pp. 147-149.

[30] R. L. Fleisher, P. B. Price, and R. M Walker, *Nuclear Tracks in Solids*, Univ. of California Press, Berkeley, (1975), pp. 562-595.

[31] A. Despic, and V. P. Parkhuitik, *Modern Aspects of Electrochemistry*, vol. 20 (1989), Plenum, New York, pp. 401.

[32] T. Nevin, O. Sadullah, K. Necmettin, Y. Hayrettin, and O. Z. Zafer, "Simple fabrication of hexagonally well-ordered AAO template on silicon substrate in two dimensions, " *Appl Phys A*. 95 (2009), pp. 781-787.

[33] H. Chik, and J. M. Xu, "Nanometric superlattices: non-lithographic fabrication, materials, and prospects, " *Mater Sci Engin R*. 43 (2004), pp. 103-138.

[34] A. P. Li, F. Muller, and U. Gosele, "Polycrystalline and Monocrystalline Pore Arrays with Large Interpore Distance in Anodic Alumina, " *Electrochem. Solid State Lett*. 3 (2000), pp. 131.

[35] A. J. Bard, and L. R. Faulkner, *Electrochemical Methods: Fundamentals and Applications*, Wiley: New York (1980).

[36] M. P. Proenca, C. T. Sousa, J. Ventura, M. Vazquez, and J. P. Araujo, "Ni growth inside ordered arrays of alumina nanopores: Enhancing the deposition rate, " *Electrochim Acta*. 72 (2012), pp. 215-221.

[37] M. P. Proenca, C. T. Sousa, J. Ventura, M. Vazquez, and J. P. Araujo, "Distinguishing nanowire and nanotube formation by the deposition current transients, " *Nano Res Lett*. 7 (2012), pp. 280.

[38] T. N. Narayanan, M. M. Shaijumon, Lijie Ci, P. M. Ajayan, and M. R. Anantharaman, "On the growth mechanism of nickel and cobalt nanowires and comparison of their magnetic properties, " *Nano Res*. 1 (2008), pp. 465-473.

[39] G. Ali, M. Ahmad, J. I. Akhter, M. Khan, K. Shafqat, M. Maqbool, and S. G. Yang, "Characterization of cobalt nanowires fabricated in anodic alumina template through AC electrodeposition, " *IEEE Trans Nanotech*. 9 (2010), pp. 223.

[40] K. Y. Kok, C. Hangarter, B. Goldsmith, I. K. Ng, N. U. Saidin, and N. V. Myung, "Template assisted growth and characterization of electrodeposited permalloy (Ni80Fe20)/Cu multi-layered nanowires, " *ECS Trans*. 25 (2010), pp. 97-103.

[41] H. P. Klug, and L. E. Alexander, *X-ray Diffraction Procedures*, Wiley, New York, pp. 125 (1962).

[42] D. J. Sellmyer, M. Zheng, and R. Skomski, "Magnetism of Fe, Co and Ni nanowires in self-assembled arrays, " *J Phys Cond Matt*. 13 (2001), pp. R433-R460.

[43] Y. L. Li, S. L. Tang, R. Xie, Y. Wang, M. Yang, J. L. Gao, W. B. Xia, and Y. W. Du, "Fabrication and magnetic properties of free-standing Ni nanotube arrays with controllable wall thickness, " *Appl Phys Lett*. 100 (2012), pp. 052402.

[44] J. Prat-Camps, C. Navau, D. X. Chen, and A. Sanchez, "Exact analytical demagnetizing factors for long hollow cylinders in transverse field, " *IEEE Magn Lett*. 3 (2012), pp. 0500104.

[45] B. Heinrich, J. F. Cochran, and F. R. Hasegawa, "FMR line broadening in metals due to two-magnon scattering, " *J Appl Phys*. 57 (1985), pp. 3690.

[46] B. Bhushan, *Springer Handbook of Nanotechnology*, Chapter -5 by H. (Mary) Shang and G. Cao, "Template-based synthesis of nanorod or nanowire arrays, " Springer (2010), pp. 169-186.